Deposition of magnetic particles: a computer simulation study

2003 J. Phys.: Condens. Matter 15 S1291

(http://iopscience.iop.org/0953-8984/15/15/301)

INSTITUTE OF PHYSICS PUBLISHING JOURNAL OF PHYSICS: CONDENSED MATTER

J. Phys.: Condens. Matter **15** (2003) S1291–S1304 PII: S0953-8984(03)54817-2

Deposition of magnetic particles: a computer simulation study

F de los Santos[1,2], M Tasinkevych[2], J M Tavares[2,3] and P I C Teixeira[4,5]

[1] Physics Department, Boston University, 590 Commonwealth Avenue, Boston, MA 02215, USA
[2] Centro de Física Teórica e Computacional da Universidade de Lisboa, Avenida Professor Gama Pinto 2, P-1649-003 Lisbon, Portugal
[3] Departamento de Ciências Exactas e Tecnológicas, Universidade Aberta, Rua Fernão Lopes 9, 2º Dto, P-1000-132 Lisbon, Portugal
[4] Faculdade de Engenharia, Universidade Católica Portuguesa, Estrada de Talaíde, P-2635-631 Rio de Mouro, Portugal
[5] Departamento de Engenharia de Materiais and Instituto de Ciência e Engenharia de Materiais e Superfícies, Instituto Superior Técnico, Avenida Rovisco Pais, P-1049-001 Lisbon, Portugal

Received 15 October 2002
Published 7 April 2003
Online at stacks.iop.org/JPhysCM/15/S1291

Abstract

We report a Monte Carlo simulation of deposition of magnetic particles on a one-dimensional substrate. Incoming particles interact with those that are already part of the deposit via a dipole–dipole potential. The strength of the dipolar interaction is controlled by an effective temperature T^*, the case of pure diffusion-limited deposition being recovered in the limit $T^* \to \infty$. Preliminary results suggest that the fractal dimension of the deposits does not change with temperature but that there is a (temperature-dependent) crossover from regimes of temperature-dependent to universal behaviour. Furthermore, it was found that dipoles tend to align with the local direction of growth.

1. Introduction

Magnetic particles are a key ingredient of many modern data recording and storage devices, from music tapes to computer hard disks [1]. For these applications smooth, regular magnetic layers are usually desired. However, dipoles, both magnetic and electric, display a fondness for arranging themselves into highly inhomogeneous structures. This is a consequence of the very strong anisotropy of the dipole–dipole interaction, which couples the orientations of the dipole moments with that of the interparticle vector. Because the potential energy at a fixed separation is lowest for a head-to-tail geometry, chain formation is particularly favoured in ferrofluids (dispersions of ferromagnetic particles) [2] or electrorheological fluids (dispersions of highly polarizable particles in solvents with low dielectric constant) [3] in magnetic and electric fields, respectively. Whether such chaining can occur in zero field in the absence of any interactions other than dipolar is experimentally uncertain; it has been seen in simulations,

but is not yet fully accounted for theoretically. Likewise, what is the true equilibrium structure of a solid of hard magnetic particles is still unsettled (see, e.g., [4] and references therein).

It is therefore of great importance, from a practical as well as from a fundamental point of view, to investigate the influence of true long-range magnetic dipolar forces on the geometry of particle aggregates, so as to be able to exert better control over them. This is especially relevant to the very novel field of self-assembled nanostructured magnetic materials, where the aim is to allow different microscopic components to organize themselves into complex functional patterns once their interactions have been appropriately tailored [1, 5]. Many of these devices, either existing or at the design stage, have low dimensionalities (e.g., wires and films), at which simulations of model systems have revealed the chaining tendency to be particularly strong [6–9].

To our knowledge, there is only one detailed study of how dipolar interactions alone affect growth. Pastor-Satorras and Rubí [10] simulated an off-lattice, two-dimensional (2D) particle–cluster aggregation model. They found a monotonic variation of the fractal dimension of the aggregates as a function of temperature (i.e., dipole strength), the limit of diffusion-limited aggregation (DLA) being recovered at high temperatures. In addition, a separate investigation by the same authors has shown that highly structured layers could be obtained at low temperatures by sequential adsorption of dipolar particles [11]. See also [12, 13] for related work on other systems.

Here we report on a simulation of dipole deposition on a one-dimensional (1D) substrate (i.e., a line). In the limit of zero magnetic moment this reduces to diffusion-limited deposition (DLD), which should exhibit the same geometrical properties as DLA [14]; our work thus serves as a both a check and an extension of Pastor-Satorras and Rubí's to the case of an infinite (in one spatial dimension) system. In particular, we want to ascertain: firstly, whether the fractal dimension actually changes owing to the strong anisotropy of the dipolar interaction: and, secondly, what is the correlation between the orientations of dipoles in the aggregate and its direction(s) of growth. For computational convenience our dipoles are restricted to residing at the sites of a 2D square lattice (although they can point in any direction of three-dimensional (3D) space): we assume that any effects coming from this discretization of space are much smaller than those of the interparticle potential. That this should be so is suggested by results for DLA [15] (but remains of course to be confirmed by full off-lattice calculations). Furthermore, our analysis in terms of the concepts of fractal geometry presumes that *all* our deposits are self-similar over some length scale larger than the mesh spacing but smaller than the deposit size [14]; again, this need not be true of the smallest deposits, but these contain only a very small fraction of the total number of particles.

The present paper is a natural progression to non-equilibrium processes from our earlier researches on the thermodynamics and phase equilibria of dipolar fluids [4]. It is organized as follows: in section 2 we describe our model and the simulation method employed. Then in section 3 we present and discuss our results, specifically comparing them with those of Pastor-Satorras and Rubí [10]. Section 4 summarizes our findings and outlines prospects for future research. Technical details pertaining to the treatment of the long range of the dipole–dipole interaction are relegated to two appendices.

2. Model and simulation method

Our simulations were performed on a (1 + 1)-dimensional square lattice of width $L = 800a$ sites and any height that can accommodate N dipoles, where a is the mesh spacing and the adsorbing substrate coincides with the bottom row (henceforth we take $a = 1$). Periodic boundary conditions are imposed in the direction parallel to the substrate. Each particle carries a 3D dipole moment of strength $\boldsymbol{\mu}$ and they interact through the pair potential

$$\phi_D(1,2) = -\frac{\mu^2}{r_{12}^3}[3(\hat{\mu}_1 \cdot \hat{r}_{12})(\hat{\mu}_2 \cdot \hat{r}_{12}) - \hat{\mu}_1 \cdot \hat{\mu}_2], \qquad r_{12} \geqslant a, \tag{1}$$

where r_{12} is the distance between particles 1 and 2, $\hat{r}_{12}$ is the 2D unit vector along the interparticle axis, and $\hat{\mu}_1$ and $\hat{\mu}_2$ are the 3D unit vectors in the direction of the dipole moments of particles 1 and 2 respectively. Finally, '1' and '2' denote the full set of positional and orientational coordinates of particles 1 and 2.

A particle is introduced at a lattice site $(x_{in}, H_{max} + AL)$, where x_{in} is a random integer in the interval $[1, L]$, H_{max} is the maximum distance from the substrate to any particle in the deposit, and A is a constant. The dipole moment of the released particle is oriented at random. The particle then undergoes a random walk by a series of jumps to nearest-neighbour lattice sites, while experiencing dipolar interactions with the particles that are already attached to the deposit. We incorporate the effects of these interactions through a Metropolis algorithm. If the deposit contains N particles, then the interaction energy of the $(N+1)$th incoming particle (the random walker) with the particles in the deposit is given by $E(\boldsymbol{r}, \hat{\mu}) = \sum_{i=1}^{N} \sum_{n}^{\infty} \phi_D(i, N+1)$, where $\boldsymbol{r}$ and $\hat{\mu}$ are the current position and the dipole orientation of the random walker respectively ($\boldsymbol{r}$ is a 2D vector). Then we randomly choose a new position $\boldsymbol{r}'$ ($|\boldsymbol{r} - \boldsymbol{r}'| = a$) and a new dipole orientation $\hat{\mu}'$ for the random walker; this displacement is accepted with probability

$$p = \min\left\{1, \exp\left[-\frac{E(\boldsymbol{r}', \hat{\mu}') - E(\boldsymbol{r}, \hat{\mu})}{T^*}\right]\right\}. \tag{2}$$

$T^* = k_B T a^3/\mu^2$ is an effective temperature, inversely proportional to the dipolar energy scale. In the limit $T^* \to 0$ only displacements that lower the energy $E(\boldsymbol{r}', \hat{\mu}')$ are accepted. On the other hand, in the limit $T^* \to \infty$ all displacements are accepted and our model reduces to the well-known DLD [14].

The long range of the dipole–dipole interaction was treated by the Ewald sum method (see appendix A for details). In our simulations we set $\alpha = 10/L$, for which it suffices to retain terms with $n = 0$ in the real-space sum of equation (A.11). The sum in reciprocal space extends over all lattice points $k = 2\pi n/L$ with $|n| \leqslant 16$, whereas the sum in real space is truncated at $L/2$.

The particle eventually either contacts the deposit (i.e., becomes a nearest neighbour of another particle that is already part of the deposit) or moves away from the substrate. In the latter case, if the particle reaches a distance from the substrate greater than $H_{max} + 2AL$, it is removed and a new one is launched. Once a particle has reached the substrate or the deposit, its dipole relaxes along the direction of the local field created by all other particles in the deposit. In all simulations reported here we took $A = 1$; larger values of A were tested and found to give the same results, but with drastically increased computation times.

3. Results and discussion

Four effective temperatures were considered: $T^* = 10^{-1}$ (28 deposits), 10^{-2} (41 deposits), 10^{-3} (42 deposits), and 10^{-4} (54 deposits), chosen to be in the range where the fractal dimension of dipolar DLA clusters is expected to change [10]. Each deposit contains 50 000 dipoles. We have also generated 30 DLD deposits on the same lattice by this same method, with $T^* = \infty$; known results for DLD (see, e.g., [16]) were used to check the validity of our algorithm. On the other hand, comparison between these and the results for finite temperatures reveal the effect of dipolar interactions on DLD.

Figure 1 is a snapshot of two deposits for $T^* = 10^{-1}$ (black) and $T^* = 10^{-4}$ (grey; only part of the deposit is shown—in fact, it grows up to a height of about 8000). The two

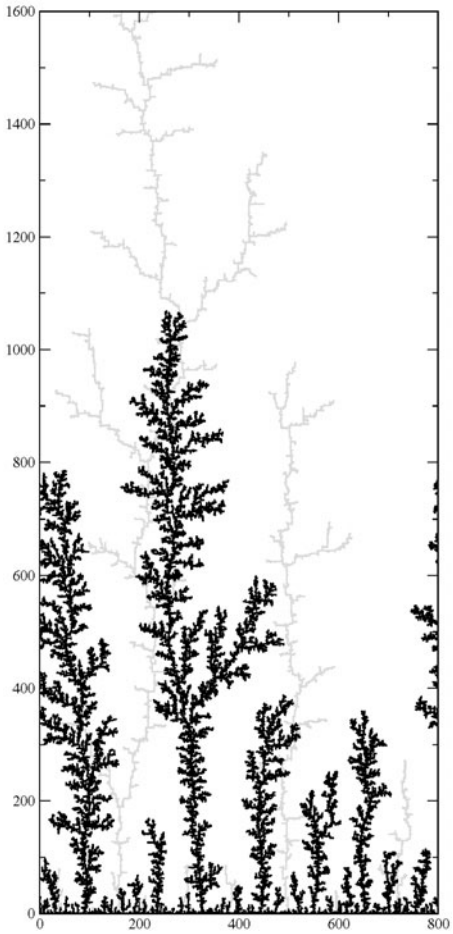

Figure 1. Snapshots of two deposits obtained for $T^* = 10^{-1}$ (black) and $T^* = 10^{-4}$ (grey).

deposits have the same general appearance, already observed in DLD: they consist of several trees competing to grow. As the size of the deposit increases, fewer and fewer trees 'survive' (i.e., carry on growing), as a consequence of the so-called shielding or screening effect. From figure 1 this seems more pronounced at lower temperatures, since above a height of 1000 (about 1/8 of the maximum height attained by this deposit) only one tree survives.

In order to compare quantitatively the results obtained for different temperatures we have measured the mean density of dipoles $\rho(h)$ at a height h,

$$\rho(h) = \left\langle \frac{1}{L} \sum_{i=1}^{L} \eta(i,h) \right\rangle, \tag{3}$$

where $\eta(i,h)$ is 1 (0) if the site with coordinates (i,h) is occupied (unoccupied), and the average (denoted by angular brackets) is taken over all available deposits at each temperature. $\rho(h)$ is plotted in figure 2(a): all the curves have similar shapes, with a smooth decrease at small h, levelling off (saturating) at intermediate h, and with a sharp drop at large h, when the top of the deposit is reached. It is immediately noticed that the finite-temperature curves differ from that for DLD in one important respect: the density at a given height and the maximum

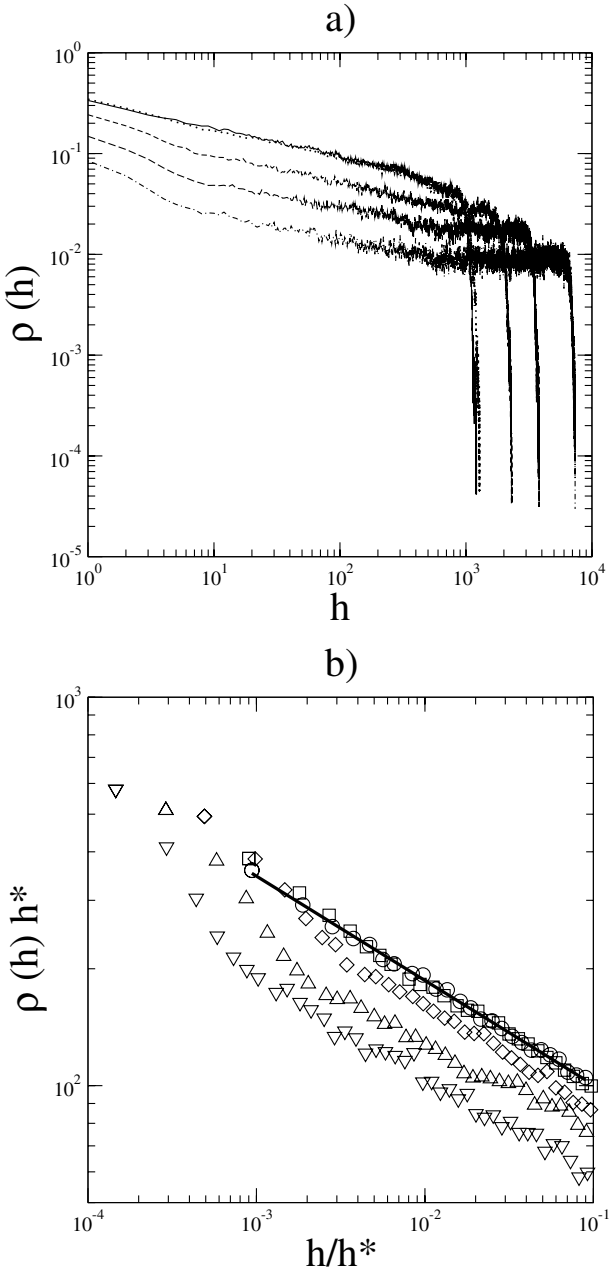

Figure 2. (a) The mean density $\rho(h)$ of deposits at height h: random deposition (solid curve), $T^* = 10^{-1}$ (dotted curve), 10^{-2} (dashed curve), 10^{-3} (long-dashed curve), and 10^{-4} (dot–dashed curve). (b) $h^*\rho(h)$ versus h/h^*: random deposition (circles), $T^* = 10^{-1}$ (squares), 10^{-2} (diamonds), 10^{-3} (upward-pointing triangles), and 10^{-4} (downward-pointing triangles). The solid line is a linear fit to the DLD results in the range of the graph; it has slope -0.28.

height h^* attained by the deposits vary with temperature. These variations are monotonic: $\rho(h)$ is smaller and h^* is larger at lower temperatures and thus the increase in the strength of dipolar interactions enhances the shielding effect.

For DLD, $\rho(h)$ was found to be of the form [14]

$$\rho(h) \propto h^{-\alpha} g(h/h^*), \tag{4}$$

where α, the so-called codimensionality, is the difference between the dimension of space d (=2, in the present case) and the fractal dimension D of the deposit, h^* is the maximum height, and $g(x)$ is a universal function. $g(x) \approx 1$ when $x \ll 1$ and decays faster than any power of x when $x \to 1$. In order to compare DLD and finite-temperature results, we propose a general form for $\rho(h)$, inspired by equation (4):

$$\rho(h, T^*) = A(T^*) h^{-\alpha} g(h/h^*), \tag{5}$$

where $A(T^*)$ is some unknown function of T^* only. It is easily seen that $A(T^*)$ can be found as a function of h^* and of the number of particles in the deposit N, by using the normalization condition

$$N = L \sum_{h=1}^{h^*} \rho(h, T^*) \approx L \int_1^{h^*} \rho(h, T^*)\, \mathrm{d}h, \tag{6}$$

whence

$$A(T^*) = \frac{N h^{*(\alpha-1)}}{L \int_{1/h^*}^1 x^{-\alpha} g(x)\, \mathrm{d}x}. \tag{7}$$

Since $g(x)$ is a universal function and L and N are the same for all the deposits that we are analysing, equation (5) becomes

$$\rho(h, T^*) h^* \propto \left(\frac{h}{h^*}\right)^{-\alpha} g(h/h^*). \tag{8}$$

In figure 2(b) we plot $h^* \rho(h, T^*)$ as a function of h/h^*, for $h/h^* \ll 1$ on a log–log scale. The data points for DLD follow, as expected, a straight line. A linear regression gives $\alpha \approx 0.27$ and thus $D \approx 1.73$, in good agreement with what was obtained previously by several other methods [16, 17]. If the full functional dependence of $\rho(h, T^*)$ were captured by equation (5), two possibilities would arise:

(i) α is T^*-independent and all curves are parallel straight lines;
(ii) α depends on T and all curves are straight lines with different slopes.

However, we arrive at neither of these scenarios, so the situation is a little more complex. If we were to interpret our results in terms of a function similar to equation (5), then $g(x)$ would also need to have an explicit temperature dependence. This dependence should be able to describe the trends observed in figure 2(b) for finite temperatures: a crossover between an approximately linear regime for very low relative heights, characterized by an exponent greater than $\alpha = 0.27$; and a linear regime for intermediate heights, characterized by roughly the same exponent as DLD.

In [10] it was argued that the change in the conformational properties of DLA clusters introduced by the presence of dipolar interactions could be interpreted as a change in their fractal dimension. The fractal dimension for each temperature was determined by measuring the dependence of the radius of gyration of dipolar DLA clusters on the number of particles in a cluster. Between $T^* = 10^{-1}$ and 10^{-4} a fractal dimension was obtained ranging from about 1.7 to 1.2. We have performed linear fits to the data shown in figure 2(b), using only those points corresponding to heights below the region where the crossover referred to above seems to take place. These points follow straight lines with temperature-dependent slopes ranging from 0.3 (for $T^* = 10^{-1}$) to 0.6 (for $T^* = 10^{-4}$). On the basis of the analysis of

just this part of the deposit, we obtain an (apparent) variation of the fractal dimension of the deposits with T^*, from $D = 1.7$ to 1.4. We conclude, as was already pointed out in [14] and seems to be confirmed by the present work, that the results of [10] can be interpreted in terms of a crossover between a temperature-dependent fractal dimension at short length scales, to $D \approx 1.7$ at long length scales, with a crossover height that itself depends on temperature. This conclusion must, however, be tested with longer simulations at the lowest temperatures, where the statistics are a little poorer.

There are other routes to estimating the fractal dimension of the deposits. We shall use one other to show that it is not necessary to assume that the finite-temperature deposits have a fractal dimension different from DLD. The mean height of the upper surface, h_m, when the deposit contains M particles, is defined as [16]

$$h_m(M) = \left\langle \frac{1}{L} \sum_{i=1}^{L} h_{max}(i, M) \right\rangle, \tag{9}$$

where $h_{max}(i, M)$ is the maximum height of the occupied sites of column i when there are M particles in the deposit. In a DLD deposit this quantity is expected to scale with M, as [16]

$$h_m \propto M^{\phi}. \tag{10}$$

The exponent ϕ is related to the codimensionality $\alpha = d - D$ by $\phi = \frac{1}{1-\alpha}$ and to the fractal dimension by $D = d - 1 + \phi^{-1}$. In figure 3 we plot our results for $h_m(M)$. The scaling law, equation (9), is known to be valid in the limit $M \to \infty$ [16]. As in [16], we have performed several linear regressions for large M, in the range $M_1 < M < M_2$, for $(M_1, M_2) = (0.5N, N)$, $(0.25N, N)$, $(0.1N, N)$, and $(0.25N, 0.5N)$ (recall that $N = 50\,000$). For every temperature and every range considered we found that $1.33 < \phi < 1.44$, which corresponds to a fractal dimension, $1.69 < D < 1.75$. Moreover, we have found no evidence of any regular variation of ϕ with T^* over a given range of M. Figure 3(a) shows that, in the initial stages of growth, the mean height of the upper surface grows identically at every temperature. There is then a crossover region at intermediate stages when the less dense deposits grow slightly faster. Finally, in the later stages all the deposits grow at the same rate regardless of temperature, as evidenced by figure 3(b). However, note that, as is clear from figure 3(a), if the deposits had been allowed to grow only to intermediate stages (e.g., up to $M = 10\,000$), an increasing value of ϕ with increasing temperature would have obtained, and thus an apparent variation of D with T^*, with the same trends as observed through the calculation of $\rho(h)$.

We conclude this analysis by attempting to make a first connection between the orientation of the dipoles in the deposit and its growth. Figure 4 is a snapshot of part of a deposit for $T^* = 10^{-1}$. Dipoles whose horizontal (or lateral) component is smaller (greater) in absolute value than their vertical component are shown in black (grey). Since we have verified that the z-component (i.e., out-of-plane component) of the dipoles in the deposit is zero after a short time, figure 4 suggests that the dipoles tend to align with the direction of growth of the deposit at the site where they attach. In order to make this idea more quantitative, we have measured the angles ω between the direction of the dipole moments of all incoming particles and the direction of growth at their point of attachment to the deposit. We have done so by recording whether a new dipole becomes attached to the substrate due to a neighbour positioned to its left or to its right (lateral growth: the relevant angle is that between the dipole and the horizontal axis), or above or below it (vertical growth: the relevant angle is now that between the dipole and the vertical axis). We did not take into account particles that attach to the deposit having both vertical and horizontal neighbours. Once these angles were collected, for every deposit at each temperature, we constructed a frequency histogram by dividing the interval $(-\pi, \pi)$ into 1000 sub-intervals. In figure 5 we plot these results for lateral and vertical growth at $T^* = 10^{-1}$

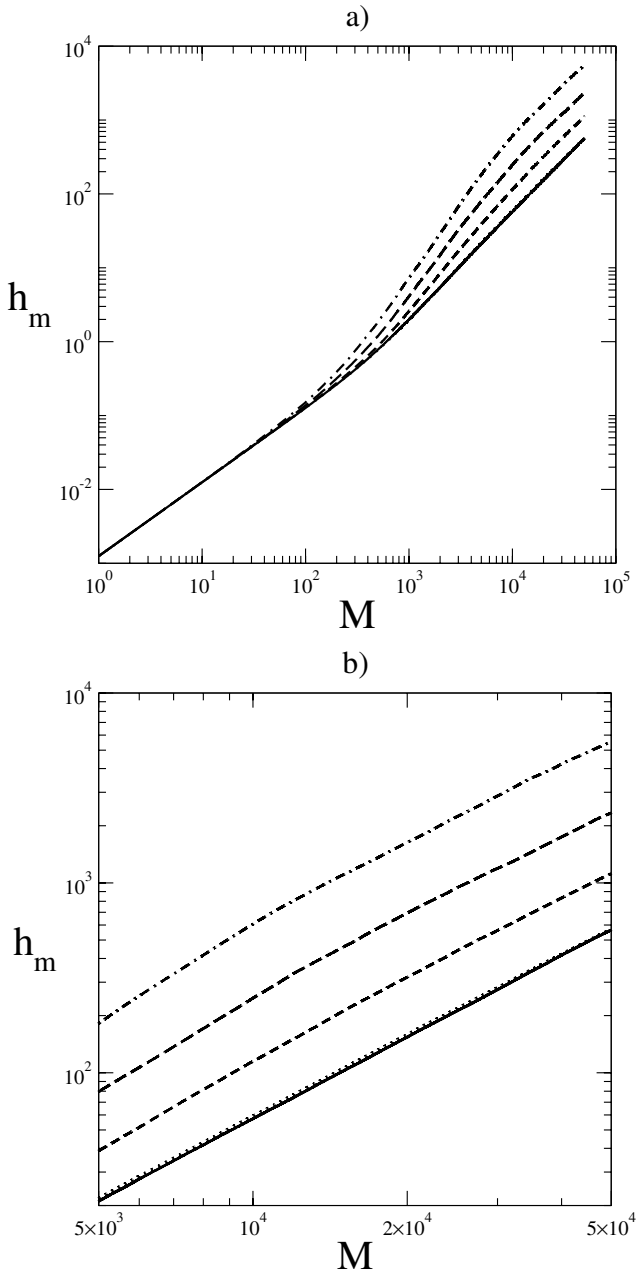

Figure 3. (a) Mean height of the upper surface, h_m, as a function of the number of particles, M. The lines are as in figure 2(a). (b) A blow-up of the large-M region.

and 10^{-4}. Because all curves have period π and are even, only the interval $(-\pi/2, \pi/2)$ is shown. The main feature of all the curves is the strong peaks at $\omega = 0$, implying that most dipoles align in the direction of growth of the deposit. This is a consequence of the fact that the lowest-energy configuration of two dipoles a fixed distance apart is head-to-tail along the direction of the interdipole vector. These peaks are more pronounced at the lower temperature,

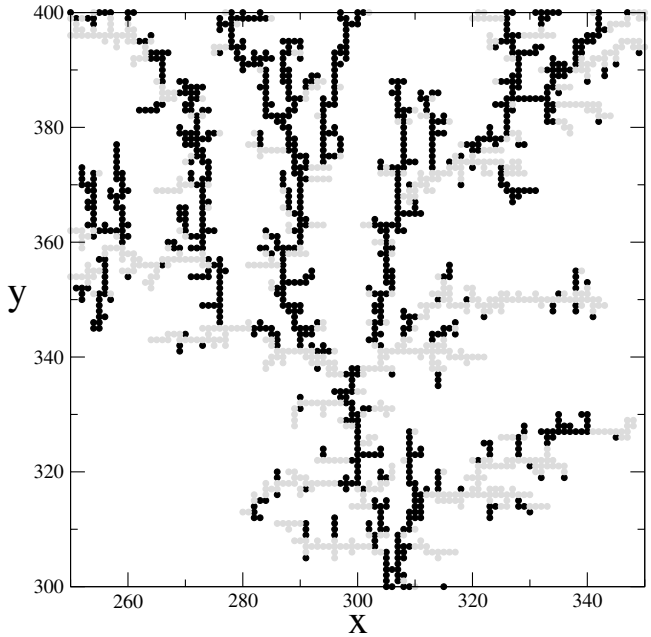

Figure 4. Detail of a deposit for $T^* = 10^{-1}$. Sites whose dipoles make an angle of absolute value smaller (larger) than $\pi/4$ with the vertical axis are shown in black (grey).

and the peak for vertical growth is a little higher than that for lateral growth at both temperatures, implying that growth in the vertical direction is more likely to happen with dipoles aligned vertically than growth in the lateral direction with dipoles aligned horizontally.

The curves exhibit some other, lower, peaks. There is a broad, low peak around $\omega = \pi/2$ at $T^* = 10^{-1}$, which corresponds to lateral growth with vertically aligned dipoles ('black' horizontal branches in figure 4), or to vertical growth with horizontally aligned dipoles ('grey' vertical branches in figure 4), at high temperatures. This can be explained by noting that the second-lowest minimum of the interaction energy at fixed separation is for two antiparallel dipoles. These peaks seem to disappear at $T^* = 10^{-4}$, suggesting that energetic effects become more important as the temperature is lowered.

There are several other peaks, occurring at the same angles for both lateral and vertical growth, whose positions seem unaffected by changing the temperature. At the present stage of our work, we can only speculate as to their origin. We believe these peaks come from a combination of lattice effects and the properties of the dipolar interaction. It is actually known that the minimum-energy arrangement of n ($\geqslant 3$) dipoles is obtained by placing them at the vertices of a regular n-sided polygon, tangent to the circumscribing circle. Thus four dipoles on a square lattice will minimize their energy by making $\pi/4$ angles with the horizontal and vertical axes, which might explain the peaks observed in figure 4 at that angle. The remaining peaks may likewise correspond to other arrangements of dipoles realizing other minima of the energy of sets of dipoles on a square lattice.

4. Concluding remarks

We have simulated the deposition of dipolar particles on a 1D substrate using a lattice model. Our findings suggest that the fractal dimension of the deposits is the same as for DLD

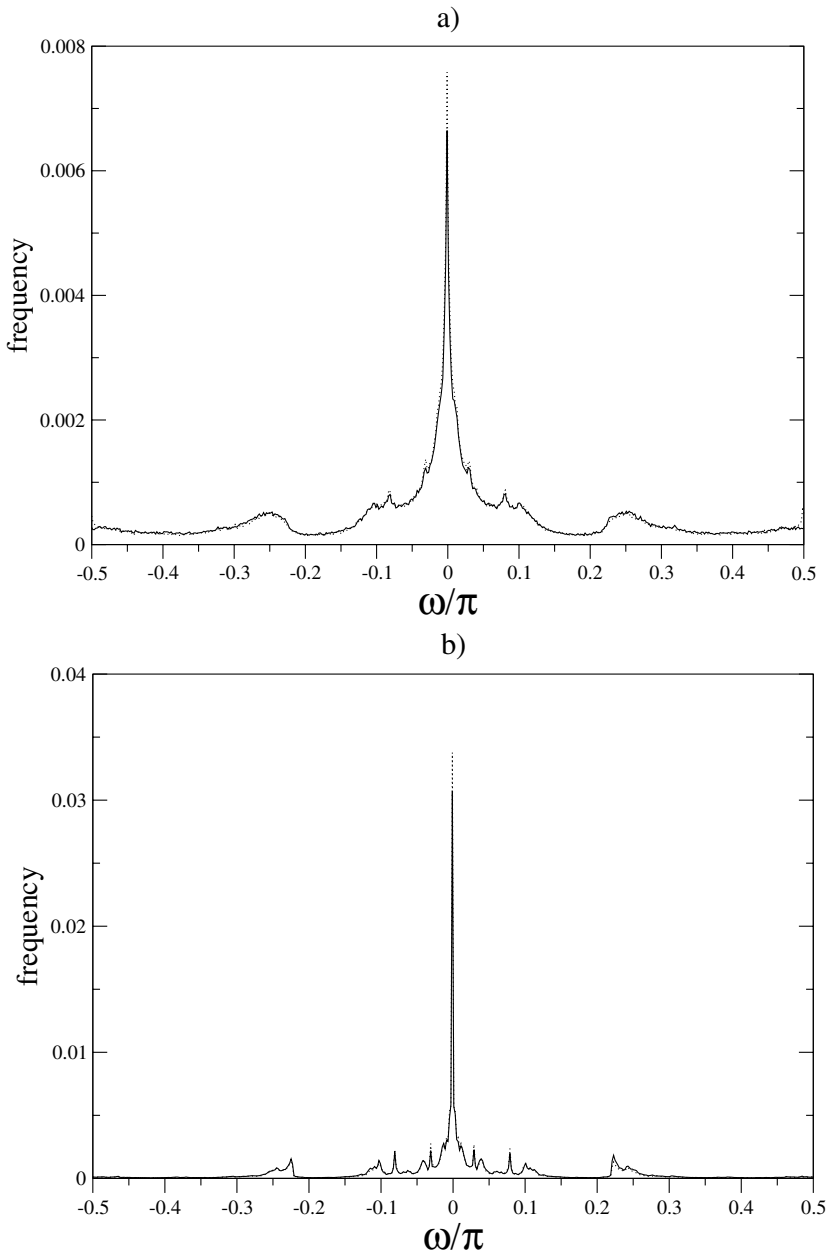

Figure 5. Frequency histograms of the angle ω between dipole orientation and the local direction of growth, for (a) $T^* = 10^{-1}$ and (b) $T^* = 10^{-4}$. The solid curves correspond to lateral growth and the dotted curves to vertical growth.

and hence unaffected by the dipolar interactions, but also that there is a crossover from temperature-dependent to temperature-independent behaviour which can be very broad. A fuller characterization in terms of the height–height correlation function, tree size distributions, and density scaling with system size is in progress and will be published elsewhere.

These quantities would provide additional routes to the fractal dimension, thus allowing us further to verify (or disprove) our preliminary conclusions. Growth and roughness exponents will also be calculated.

We have now started work on the off-lattice version of the present model, so as to be free from any possible artifacts arising from the discretization of space. Results so far suggest that the lattice has a very small effect, but we are currently somewhat limited by the very high computational cost of evaluating the interactions between a particle and all its periodic images at every step. More efficient algorithms are being developed to tackle this.

Acknowledgments

Funding from the Fundação para a Ciência e Tecnologia (Portugal) is gratefully acknowledged—in the form of post-doctoral fellowships Nos SFRH/BPD/5654/2001 (F de los Santos) and SFRH/BPD/1599/2000 (M Tasinkevych) and partial support (P I C Teixeira). We thank M M Telo da Gama for helpful discussions and J J Weis for advice on how to treat the Ewald sums.

Appendix A. Ewald sums for the deposition process

We have generalized to arbitrary dimensions a method proposed by Grzybowski *et al* [18] for evaluating Ewald sums. Here for simplicity we just present results for our case $d = 1$ (where d is the number of dimensions in which we impose periodic boundary conditions). Our simulation box consists of a rectangle with a base of length L and any height that can accommodate N dipoles. The dipoles $\boldsymbol{\mu}_i$ are always 3D vectors, with position vectors $\boldsymbol{R}_i$, $i = 1, 2, \ldots, N$. The simulation box is repeated in the $\boldsymbol{x}$-direction (horizontal), giving rise to a regular lattice whose sites are located at $\boldsymbol{n} = (n, 0)L$. Let $\boldsymbol{\mu}$ and $\boldsymbol{R}$ be the dipole moment and position of an incoming particle. Then, the distance between the incoming particle in the origin cell and another in an image cell is $\boldsymbol{r}_i \equiv \boldsymbol{R} - (\boldsymbol{R}_i + \boldsymbol{n})$, $i = 1, 2, \ldots, N$. The total interaction energy between the incoming particle and the N particles in the box and their infinite replicas is

$$E = \sum_{i=1}^{N} \sum_{\boldsymbol{n}}^{\infty} \left\{ \frac{\boldsymbol{\mu} \cdot \boldsymbol{\mu}_i}{|\boldsymbol{r}_i + \boldsymbol{n}|^3} - 3 \frac{[\boldsymbol{\mu} \cdot (\boldsymbol{r}_i + \boldsymbol{n})][\boldsymbol{\mu}_i \cdot (\boldsymbol{r}_i + \boldsymbol{n})]}{|\boldsymbol{r}_i + \boldsymbol{n}|^5} \right\}. \tag{A.1}$$

According to the geometry of the system, $\boldsymbol{r}_i = (x_i, y_i, 0)$ where x_i (y_i) is the horizontal (vertical) distance between the incoming particle and a particle in the deposit. Note that the incoming particle does not interact with its own images.

Introducing the notation

$$\psi(\boldsymbol{r}) = \sum_{\boldsymbol{n}} \frac{1}{|\boldsymbol{n} + \boldsymbol{r}|^3}, \qquad \boldsymbol{r} \neq \boldsymbol{0}, \tag{A.2}$$

$$\theta(\boldsymbol{r}, \boldsymbol{c}) = \sum_{\boldsymbol{n}} \frac{\mathrm{e}^{-\mathrm{i}\boldsymbol{c}\cdot(\boldsymbol{n}+\boldsymbol{r})}}{|\boldsymbol{n} + \boldsymbol{r}|^5}, \qquad \boldsymbol{r} \neq \boldsymbol{0}. \tag{A.3}$$

allows us to express the total energy as

$$E = \sum_{i=1}^{N} \boldsymbol{\mu} \cdot \boldsymbol{\mu}_i \psi(\boldsymbol{r}_i) + 3 \sum_{i=1}^{N} (\boldsymbol{\mu} \cdot \boldsymbol{\nabla}_{\boldsymbol{c}})(\boldsymbol{\mu}_i \cdot \boldsymbol{\nabla}_{\boldsymbol{c}}) \theta(\boldsymbol{r}_i, \boldsymbol{c})|_{\boldsymbol{c}=\boldsymbol{0}}. \tag{A.4}$$

To calculate $\psi(\boldsymbol{r})$ and $\theta(\boldsymbol{r}, \boldsymbol{c})$ we use the identities

$$x^{-2u} = \frac{1}{\Gamma(u)} \int_0^{\infty} t^{u-1} \mathrm{e}^{-xt^2} \, \mathrm{d}t, \tag{A.5}$$

$$\sum_{n} \mathrm{e}^{-t|r+n|^2-\mathrm{i}c\cdot(r+n)} = \left(\frac{\pi}{tL^2}\right)^{1/2} \sum_{k} \mathrm{e}^{\mathrm{i}k\cdot r} \exp\left(-\frac{(k+c)^2}{4t}\right). \tag{A.6}$$

$k = 2\pi(k,0)/L$ with k integer is a reciprocal-lattice vector and r and n are as above. Equation (A.5) is a direct consequence of the definition of the gamma function, while equation (A.6) is a form of the Poisson summation formula for $d = 1$, which is the dimensionality of the lattice formed by repeating the box.

For $\psi(r)$ we set $u = 3/2$, leading to

$$\psi(r) = \frac{1}{\Gamma(3/2)} \sum_{n} \int_0^\infty t^{1/2} \mathrm{e}^{-|r+n|^2 t}\, \mathrm{d}t. \tag{A.7}$$

The sum over direct-lattice vectors converges fast for large t, while that over reciprocal-lattice vectors does so for small t. We therefore choose an arbitrary separation parameter α^2 for the t-integration and decompose the lattice sum into two terms:

$$\psi(r) = \frac{2}{\sqrt{\pi}} \sum_{n} \int_{\alpha^2}^\infty t^{1/2} \mathrm{e}^{-t|r+n|^2}\, \mathrm{d}t + \frac{2}{\sqrt{\pi}} \sum_{n} \int_0^{\alpha^2} t^{1/2} \mathrm{e}^{-t|r+n|^2}\, \mathrm{d}t. \tag{A.8}$$

Taking into account that $-t|r+n|^2 = -t|x+n|^2 - ty^2$ and using the Poisson summation formula, equation (A.6), we arrive at

$$\psi(r) = \frac{2}{\sqrt{\pi}} \sum_{n} \int_{\alpha^2}^\infty t^{1/2} \mathrm{e}^{-t|r+n|^2}\, \mathrm{d}t + \frac{2\sqrt{\pi}}{L} \sum_{k} \mathrm{e}^{-\mathrm{i}kx} \int_0^{\alpha^2} \exp\left(-ty^2 + \frac{k^2}{4t}\right) \mathrm{d}t. \tag{A.9}$$

In the case of $\theta(r, c)$ we set $u = 5/2$ with the result

$$\begin{aligned}\theta(r,c) = {} & \frac{1}{\Gamma(5/2)} \sum_{n} \mathrm{e}^{-\mathrm{i}c\cdot(r+n)} \int_{\alpha^2}^\infty t^{3/2} \mathrm{e}^{-t|r+n|^2}\, \mathrm{d}t \\ & + \frac{4}{3L} \sum_{k} \mathrm{e}^{\mathrm{i}kx - \mathrm{i}yc_y} \int_0^{\alpha^2} t \exp\left(-ty^2 + \frac{k^2}{4t}\right) \mathrm{d}t. \end{aligned} \tag{A.10}$$

We now substitute $\psi(r)$ and $\theta(r, c)$ into equation (A.4) for E:

$$\begin{aligned} E = {} & \frac{2}{\sqrt{\pi}} \sum_{i} \sum_{n} \left\{ (\mu\cdot\mu_i) I_{1/2}(\alpha,\beta) - 2[\mu\cdot(r_i+n)][\mu_i\cdot(r_i+n)] I_{3/2}(\alpha,\beta) \right\} \\ & + \frac{2}{L} \sum_{i} \sum_{k} (\mu_y\mu_{iy} + \mu_z\mu_{iz}) \mathrm{e}^{\mathrm{i}kx_i} J_0(\alpha, y_i, k) \\ & - \frac{4}{L} \sum_{i} \sum_{k} \mu_y\mu_{iy} y_i^2 \mathrm{e}^{\mathrm{i}kx_i} J_1(\alpha, y_i, k) \\ & + \frac{1}{L} \sum_{i} \sum_{k\neq 0} \mu_x\mu_{ix} k^2 \mathrm{e}^{\mathrm{i}kx_i} J_{-1}(\alpha, y_i, k) \\ & + \mathrm{i}\frac{2}{L} \sum_{i} \sum_{k\neq 0} k(\mu_x\mu_{iy} + \mu_{ix}\mu_y) y_i \mathrm{e}^{\mathrm{i}kx_i} J_0(\alpha, y_i, k), \end{aligned} \tag{A.11}$$

where $\beta = |r_i + n|$ and the integrals are given by (see appendix B for details)

$$I_{1/2}(\alpha, |r_i+n|) = \frac{\alpha \mathrm{e}^{-|r_i+n|^2\alpha^2}}{|r_i+n|^2} + \frac{\sqrt{\pi}}{2|r_i+n|^3} \operatorname{erfc}(\alpha|r_i+n|), \tag{A.12}$$

$$I_{3/2}(\alpha, |r_i+n|) = \frac{\alpha \mathrm{e}^{-|r_i+n|^2\alpha^2}}{|r_i+n|^2} \left(\alpha^2 + \frac{3}{2|r_i+n|^2}\right) + \frac{3\sqrt{\pi}}{4|r_i+n|^5} \operatorname{erfc}(\alpha|r_i+n|),$$

$$J_\nu(\alpha, y_i, k) = \int_0^{\alpha^2} t^\nu \mathrm{e}^{-ty_i^2 - k^2/4t}\, \mathrm{d}t. \tag{A.13}$$

Since E is real, equation (A.11) can be further simplified by replacing $\exp(\mathrm{i}kx_i)$ by $\cos(kx_i) + \mathrm{i}\sin(kx_i)$. Note also that it is even in k and that the case $k = 0$ can be treated analytically. Therefore, no distinction is made in the code between simulation box images with positive and negative k, and the case $k = 0$ is considered separately.

Appendix B. Evaluation of some relevant integrals

The following definitions and results will be useful:

$$\int_0^\infty \mathrm{e}^{-\nu t^2}\,\mathrm{d}t = \frac{1}{2}\sqrt{\frac{\pi}{\nu}}, \tag{B.1}$$

$$\mathrm{erf}(u) \equiv \frac{2}{\sqrt{\pi}}\int_0^u \mathrm{e}^{-t^2}\,\mathrm{d}t, \tag{B.2}$$

$$\mathrm{erfc}(u) \equiv 1 - \mathrm{erf}(u) = \frac{2}{\sqrt{\pi}}\int_u^\infty \mathrm{e}^{-t^2}\,\mathrm{d}t. \tag{B.3}$$

Two classes of integration need to be performed:

$$I_\nu(\alpha,\beta) = \int_{\alpha^2}^\infty t^\nu \mathrm{e}^{-t\beta^2}\,\mathrm{d}t, \tag{B.4}$$

$$J_\nu(\alpha,a,b) = \int_0^{\alpha^2} t^\nu \mathrm{e}^{-at-b/t}\,\mathrm{d}t. \tag{B.5}$$

We are interested in $I_{1/2}$ and $I_{3/2}$. They can be evaluated with the help of $I(-1/2)$, which is easy:

$$I_{-1/2}(\alpha,\beta) = \frac{\sqrt{\pi}}{\beta}\,\mathrm{erfc}(\alpha\beta), \tag{B.6}$$

where we have made the change of variable $t = z^2/\beta^2$. Now the cases $\nu = 1/2$ and $3/2$ can be easily found by integrating by parts:

$$I_{1/2}(\alpha,\beta) = \frac{\alpha\mathrm{e}^{-\beta^2\alpha^2}}{\beta^2} + \frac{\sqrt{\pi}}{2\beta^3}\,\mathrm{erfc}(\alpha\beta), \tag{B.7}$$

$$I_{3/2}(\alpha,\beta) = \frac{\alpha\mathrm{e}^{-\beta^2\alpha^2}}{\beta^2}\left(\alpha^2 + \frac{3}{2\beta^2}\right) + \frac{3\sqrt{\pi}}{4\beta^5}\,\mathrm{erfc}(\alpha\beta), \tag{B.8}$$

where we have resorted to the changes of variables $u = t^{1/2}$ and $u' = -\mathrm{e}^{-\beta^2 t}$. Turning next to J_ν, the values of ν that we are interested in depend on the system dimensionality. For $d = 1$, $\nu = -1, 0, 1$ and no analytical results are available, in contrast to the $d = 2$ case. One of the three integrals, however, can be expressed in terms of the other two:

$$\frac{k^2}{4}J_{-1} + J_0 - y^2 J_1 = \alpha^2 \exp\left(-y^2\alpha^2 - \frac{k^2}{4t}\right). \tag{B.9}$$

References

[1] Hadjipanayis G C (ed) 2001 *Magnetic Storage Systems Beyond 2000 (NATO ASI Series II)* vol 41 (Dordrecht: Kluwer)

[2] Rosensweig R E 1985 *Ferrohydrodynamics* (New York: Cambridge University Press)

[3] Halsey T C 1992 *Electrorheological Fluids* ed R Tao (Singapore: World Scientific)

[4] Teixeira P I C, Tavares J M and Telo da Gama M M 2000 *J. Phys.: Condens. Matter* **12** R411

[5] Himpsel F J, Ortega J E, Mankey G J and Wills R F 1998 *Adv. Phys.* **47** 511

[6] Weis J J 1998 *Mol. Phys.* **93** 361
[7] Weis J J 2002 *Mol. Phys.* **100** 579
[8] Tavares J M, Weis J J and Telo da Gama M M 2002 *Phys. Rev.* E **65** 061201
[9] Weis J J, Tavares J M and Telo da Gama M M 2002 *J. Phys.: Condens. Matter* **14** 9171
[10] Pastor-Satorras R and Rubí J M 1995 *Phys. Rev.* E **51** 5994
[11] Pastor-Satorras R and Rubí J M 1998 *Phys. Rev. Lett.* **80** 5373
[12] Yang F and Pan F 2001 *Phys. Rev.* E **64** 051402
[13] Morimoto H and Maekawa T 2000 *J. Phys. A: Math. Gen.* **33** 247
[14] Meakin P 1998 *Fractals, Scaling and Growth far from Equilibrium* (Cambridge: Cambridge University Press)
[15] Meakin P and Family F 1986 *Phys. Rev.* A **34** 2558
[16] Meakin P 1984 *Phys. Rev.* B **30** 4207
[17] Meakin P 1983 *Phys. Rev.* A **27** 2616
[18] Grzybowski A, Gwóźdź E and Brodka A 2000 *Phys. Rev.* B **61** 6706